



Enhanced electrocatalytic nitrate reduction by preferentially-oriented (100) PtRh and PtIr alloys: the hidden treasures of the ‘miscibility gap’

Matteo Duca^a, Nicolas Sacré^a, Andrew Wang^{a,b}, Sébastien Garbarino^a, Daniel Guay^{a,*}

^a Institut National de la Recherche Scientifique, INRS-Énergie, Matériaux et Télécommunications, 1650, Boulevard Lionel-Boulet, Varennes, J3X 1S2, Canada

^b Department of Chemistry, University of British Columbia, 2036 Main Mall, Vancouver, British Columbia, V6T 1Z1, Canada



ARTICLE INFO

Keywords:

Nitrate reduction
Epitaxial films
Alloys
Electrocatalysis
(100) surfaces

ABSTRACT

Bimetallic alloys of Pt and Rh or Ir were prepared with pulsed laser deposition (PLD) on a well-ordered MgO (100) substrate, leading to epitaxial growth along the [001] plane, as confirmed by surface analysis techniques. The out-of-equilibrium conditions of PLD allowed the exploration of a range of compositions for which phase separation would instead be expected. The electrochemistry of a series of PtRh and PtIr (100) alloys was investigated in 0.5 M H₂SO₄, showing a surprisingly intense electrocatalytic activity towards the reduction of nitrate for a Pt content of 21–42%. These alloys feature a lower reaction overpotential with respect to Rh and Ir while outperforming the pure metals in terms of reduction current. A detailed analysis of the voltammetric features with respect to alloy composition highlighted a correlation between hydrogen desorption and nitrate reduction activity. In addition, an optimal potential range for nitrate reduction, common to PtRh and PtIr alloys, was observed, corresponding to the potential window in which nitrate adsorption coincides with fast reduction of the key reaction intermediate NO_{ads}.

1. Introduction

Bimetallic bulk, surface, and near-surface alloys, have attracted growing attention with an eye to their applications as electrocatalysts [1–3]. Their unique features [4] are explained [2] in terms of an interplay between bifunctional catalysis, the dynamic formation of highly active surface domains, and radical alterations in the electronic structure. In fact, alloying enables one to tune the density of states (DOS) at the Fermi level and the shape of the *d*-band, which determine the chemical properties of the alloy. The rational design of alloys from first principles [3] can be implemented, provided that the alloyed elements are fully miscible. In this respect, pulsed laser deposition [5] (PLD) has emerged as a convenient, reliable approach to obtaining kinetically stable alloys at room temperature in the “miscibility gap” of the alloy phase diagram [6–10], a range of compositions in which the elements are expected to segregate. As an additional advantage, epitaxial growth on single-crystal substrates (usually metal oxides) can easily be achieved by PLD [11–13]. In this study, we combine these two features of PLD deposition to grow thin-film epitaxial (100) alloys of Pt and either Rh or Ir, showing that Pt-poor alloys display a remarkable electrocatalytic activity towards the reduction of NO₃[−] in H₂SO₄.

NO₃[−] reduction has a considerable significance in the electrochemical nitrogen cycle [14], both for its intriguing mechanistic

underpinnings and its implications for applied technology (wastewater remediation and the treatment of low-level nuclear waste) [15,16]. The reaction pathways at transition metal electrodes can be briefly described as a rate-determining step (NO₃[−] → NO₂[−]) followed by ensuing selectivity-determining reactions, such as the formation of strongly-adsorbed NO [17,18]. Adsorbed nitrate is the actual species involved in the rate-determining step [19,20]; unfortunately, the preliminary adsorption of NO₃[−] is known to be weak and heavily inhibited by other co-adsorbates such as H or HSO₄[−] [15,20]. Therefore, performing NO₃[−] reduction in H₂SO₄ poses significant challenges for metal electrodes, which strongly adsorb HSO₄[−]. In this respect, Pt(100) is of particular interest: when free of interfering adsorbates, this surface is able to reduce NO₃[−] at a lower overpotential than the other basal planes [21]. The interplay of the requirement of fast removal of adsorbed NO and sufficient nitrate coverage (discussed in details later in the paper) is strongly evident for this surface: nitrate reduction at single-crystal Pt(100) in 0.5 M HClO₄ occurs in a sharp spike at 0.32 V [21], a potential region close to the peak potential for the reduction of a NO adlayer [22]. The interest in Pt(100) is further motivated by the absence of poisoning upon adsorption of NO (an intermediate of nitrate reduction), thanks to the rapid hydrogenation of N_{ads} at Pt(100), as recently suggested by computational studies [22,23].

Among the noble metals, Rh is arguably the most active electrode

* Corresponding author.

E-mail address: guay@emt.inrs.ca (D. Guay).

material for the reduction of nitrate [15], in particular because it does not require the presence of available protons to reduce NO_3^- [24]. In addition, Rh features an easier adsorption of anions owing to its low potential of zero charge (pzc) [25]. From a more fundamental point of view, Rh has a number of valence electrons which can effectively stabilise N-containing intermediates [26]. Therefore, a preferentially-oriented (100) PtRh alloy represents, in theory, ‘the best of both worlds’ for the promotion of electrocatalytic nitrate reduction, combining the activity of Rh with the peculiar nitrate reduction reactivity of the (100) crystal plane. PtRh alloys have been widely investigated for electrocatalytic reactions of the nitrogen and the carbon cycle, such as nitrate reduction [27] and the oxidation of small organic molecules [27–31]. However, Pt and Rh are immiscible over an ample region of the alloy phase diagram (approx. between 20% and 80% Pt below 600 °C) [32].

Electrode materials (co-deposits, alloys) combining Pt and Ir have long been investigated as catalysts for electrochemical ammonia oxidation [10,33–35] and for nitrate reduction [36]. A polycrystalline $\text{Pt}_{70}\text{Ir}_{30}$ alloy has been reported to be more active than both pure metals for the reduction of NO_3^- in 0.5 M HClO_4 [36]. On the other hand, pure Ir does not match the catalytic activity of Rh, suffering from severe poisoning during the reduction of both NO and NO_3^- [20,37]. Experimental [37,38] and theoretical [26] studies have shown that Ir binds N adsorbates more strongly than Pt, and hence a Pt-Ir combination could be beneficial, so long as it does not induce increased poisoning [37]. By alloying varying amounts of Pt and Ir, the electronic structure may be fine-tuned and the catalytic response optimized; however, the Pt-Ir system features extensive phase segregation at low temperature: its miscibility gap spans the range 0 < % Pt < 65 at temperatures below 600 °C [9,10,39].

This survey of the literature on PtRh and PtIr alloys shows that large regions of the Pt-M phase diagrams remain uncharted territory. Therefore, we decided to take full advantage of the PLD technique to prepare a series of a thin-film PtM alloys characterised by a well-defined (100) crystal orientation and a range of compositions including the Pt-poor region. Electrochemical tests for NO_3^- reduction unveiled surprising features: when Rh or Ir is alloyed with 21 < % Pt < 42, nitrate reduction occurs at a lower overpotential than for each of the pure metals, and larger reduction current densities were recorded. Additionally, the deactivation during nitrate reduction at PtRh and PtIr alloys could be reversed by CO adsorption, as shown for the specific case of $\text{Pt}_{25}\text{Ir}_{75}$. These features were rationalised within the framework of the mechanism of nitrate reduction and of the electronic and structural properties of bimetallic alloys.

2. Experimental

Pulsed laser deposition (PLD) was used to prepare thin films of Pt, Rh, Ir and their alloys with a preferential (100) orientation. The procedure for Pt has been extensively described in previous publications [8,11]; specific details concerning the preparation of bimetallic alloys, Rh and Ir are as follows. The deposition was performed under low pressure ($3\cdot10^{-5}$ mbar) in a custom-made vacuum chamber, with a KrF laser beam (248 nm, 17 ns pulse width, 20 Hz, power density 3 J cm^{-2}), at a temperature of 600 °C for Ir and the PtIr series, and of 400 °C for Rh and the PtRh series.

$\text{MgO}(100)$ substrates (10 mm × 10 mm, epi polished, MTI Corporation) were previously cleaned by sonication in acetone (15 min) and in isopropanol (15 min) and dried under an argon stream.

Firstly, a nickel buffer layer was deposited on MgO by the ablation of a Ni foil (99.994%, 0.1 mm, Alfa Aesar) for 2000 pulses, corresponding to a thickness of approximately 1 nm. This preliminary step was found to enhance adherence and epitaxial growth of Pt films [8,11], and this strategy was also used for all other bi- and monometallic samples. PtIr and PtRh were deposited by focussing the laser on a custom-made iridium or a rhodium target, respectively, partially covered by a platinum foil. The target was kept in continuous rotational

and translational motion to ensure that the laser beam alternates between the Pt and the Ir or Rh domains. The ratio between the geometrical surface area of the platinum foil (99.99%, 0.1 mm, Alfa Aesar Company) and iridium (99.9%, Kurt J. Lesker Company) or Rh (99.8%, Kurt J. Lesker Company) target allowed control of the final alloy composition. For PtIr, the number of laser pulses was fixed at 20 000. Instead, 80 000 pulses were employed for PtRh: for this specific alloy, it was observed that thicker deposits were required to obtain a conductive film.

2.1. Physical characterization

Scanning electron microscopy (SEM, JEOL JSM 6300F) was used to image the surface morphology of the alloys. The bulk composition of the alloys was obtained by energy dispersive X-ray spectroscopy (EDX, Oxford Link ISIS, ATW2) at low magnification ($150 \times$). The composition, expressed as atomic %, was obtained from an average over 5 measurements performed at different locations on each sample (typical standard deviation 2–4%).

The crystallographic structure of the alloy was determined by X-ray diffraction (XRD) measurements (PANalytical X'Pert Pro diffractometer), using a Cu K α source (average λ is 1.54184 Å). The diffractograms were recorded in the Bragg-Brentano configuration (0–2θ mode) from 20° to 90° with a step size of 0.02° and a counting time of 0.5 s per step. Finally, the thicknesses of the films were evaluated by X-Ray Reflectivity (XRR) measurements performed by varying the incidence angle from 0.1° to 4°, with a step size of 0.005° and a counting time of 1 s per data point.

2.2. Electrochemical characterisation

All electrolytes were prepared with ultrapure water (Millipore Gradient, MilliQ, resistivity > 18.2 MΩ cm). High-purity reactants were obtained from various suppliers: H_2SO_4 (TraceMetal grade, Fisher), NaNO_3 (99.995%, Aldrich) and used as received. Prior to electrochemical measurements, the electrolyte solutions were purged by bubbling Ar (AirLiquide, UHP, 5.0) for at least 10 min. Argon blanketing was maintained over the solution during the experiments. A BioLogic VSP potentiostat, equipped with a low-current option, was used throughout this work. The low-current option allowed us to reduce the experimental noise; all voltammograms are plotted as recorded. A mercury-mercury sulfate reference electrode (MMSE) was employed for all experiments. To convert the potentials to RHE scale, the potential difference between the MMSE reference and a RHE electrode was measured in 0.5 M H_2SO_4 , and it was found equal to 700 mV. A Pt wire was used as counter electrode throughout this work, and it was flame-annealed and quenched in MilliQ water prior to immersion into the working electrolyte.

The thin films were studied in a one-compartment small-volume electrochemical cell as previously described [40]. All glassware was cleaned following a standard protocol: first, it was left in a $\text{KMnO}_4 + \text{H}_2\text{SO}_4$ solution overnight; then, it was thoroughly rinsed with MilliQ water. Traces of MnO_2 were removed by rinsing the glassware with a $\text{H}_2\text{O}_2 + \text{H}_2\text{SO}_4$ solution. Finally, traces of sulfate were removed by boiling the glassware in MilliQ water repeatedly.

As a pretreatment step, all thin-film electrodes were subjected to cycling in 0.5 M H_2SO_4 . We have previously shown that, for epitaxial (100) Pt films, such a pretreatment is required to clean the surface and obtain a stable voltammogram; potential cycling does not induce surface reconstruction leading to the appearance of crystal orientations other than Pt(100) [8]. The potential limits for Pt were 0.05–1.50 V vs RHE. On the other hand, a more restricted potential window was chosen for Ir, Rh and for most of their alloys with Pt.

Concerning Ir and all PtIr alloys, the upper potential was restricted to 1.10 V vs RHE to avoid loss of Ir. This value was reported in the literature for blank voltammograms of PtIr bulk alloys [36] and for the

oxidation of CO_{ads} at a nanostructured Ir electrode [41]. In this respect, it should be borne in mind that Ir single crystals do not lose their surface orientation as a result of the adsorption of oxygen-containing species [42].

In the case of Rh and Rh-rich alloys, the upper potential was restricted to 0.9 V, which corresponds to the upper potential limit selected for Rh single-crystal electrodes in order to ensure preservation of the surface order [43]. On the other hand, alloys with a Pt content $\geq 86\%$ required a pre-treatment up to 1.5 V, following the same protocol as pure Pt. Otherwise, it was not possible to achieve a stable voltammogram. It must be pointed out that a perturbation of the composition of PtRh alloys could take place above 1.3 V, which is suggested in the literature as a safe limit to avoid loss of Rh [28]. However, the evolution of the voltammetric features of the so-called hydrogen adsorption region as a function of the Pt content rule out dealloying or the formation of a pure Pt ‘skin’ (see following paragraph, and Sections 3.1 and 3.4).

The charge under the hydrogen underpotential deposition (H_{UPD}) peaks was used to calculate the electrochemically active surface area, which allowed us to normalise the measured currents. This method, which is an established procedure in electrochemistry, requires the knowledge of reference values for the charge involved in the adsorption of a monolayer (ML) of hydrogen on metal surfaces. For Pt, we referred to generally accepted [44] H_{UPD} charge for Pt(100), equal to $210 \mu\text{C cm}^{-2}$. For pure Ir, a charge of $220 \mu\text{C cm}^{-2}$ was employed, which corresponds to the charge of 1 ML of H_{UPD} , as calculated [42] and observed experimentally [45] for Ir(100). Therefore, we used this value for H_{UPD} on pure Ir as the most representative for the main surface orientation featured by the thin film, and the same reference charge was also employed for the PtIr alloys.

As for pure Rh, the value of $222 \mu\text{C cm}^{-2}$ was chosen, which is supported by measurements of the CO stripping charge at single-crystal Rh(100) electrodes [46]. On the other hand, a charge of $220 \mu\text{C cm}^{-2}$ for H_{UPD} was employed for the PtRh alloys.

The oxidative removal of adsorbed CO (“CO stripping” henceforth) was performed in $0.5 \text{ M H}_2\text{SO}_4$ according to the following protocol: first, the electrolyte was saturated with CO gas (Praxair, 5.0) by bubbling the gas for 5 min while keeping the electrode under potential control at $E = 0.08 \text{ V}$. After this, the electrolyte was purged with Ar for 40 min, always under potential control. Then, a potential sweep was performed at $v = 20 \text{ mV s}^{-1}$ to remove adsorbed CO, and additional voltammetric cycles were recorded to ensure that no change was observed with respect to the blank voltammogram before CO adsorption. CO stripping was carried out for all thin-film electrodes before performing nitrate reduction, as a further cleaning step.

Nitrate reduction was also performed in $0.5 \text{ M H}_2\text{SO}_4$; despite the known interference from the adsorption of (bi)sulphate on metal surfaces, H_2SO_4 was preferred to HClO_4 to avoid the formation of chloride from perchlorate reduction, which is known to take place at Ir and Rh [47]. The voltammetric profiles reported for nitrate reduction refer in all cases to the first recorded cycle, unless otherwise stated.

3. Results and discussion

3.1. Rh and PtRh alloys: characterisation and electrocatalytic nitrate reduction

Fig. 1 shows a synopsis of the θ - 2θ Bragg-Brentano X-ray diffraction (XRD) patterns for pure Rh and PtRh alloys prepared onto $\text{MgO}(100)$; the diffraction pattern of the substrate was discussed elsewhere [11] and it is reported in Fig. 1 for the sake of completeness. The alloy compositions mentioned throughout the paper were obtained by EDX analyses. A pure Rh deposit displays only one peak that can be ascribed to the metal film, the contribution at $2\theta = 47.68^\circ$. Reference patterns for Rh (retrieved in the database of the data analysis software PANalytical X'Pert HighScore) feature a signal at $2\theta = 47.782^\circ$ (JCPDS No.

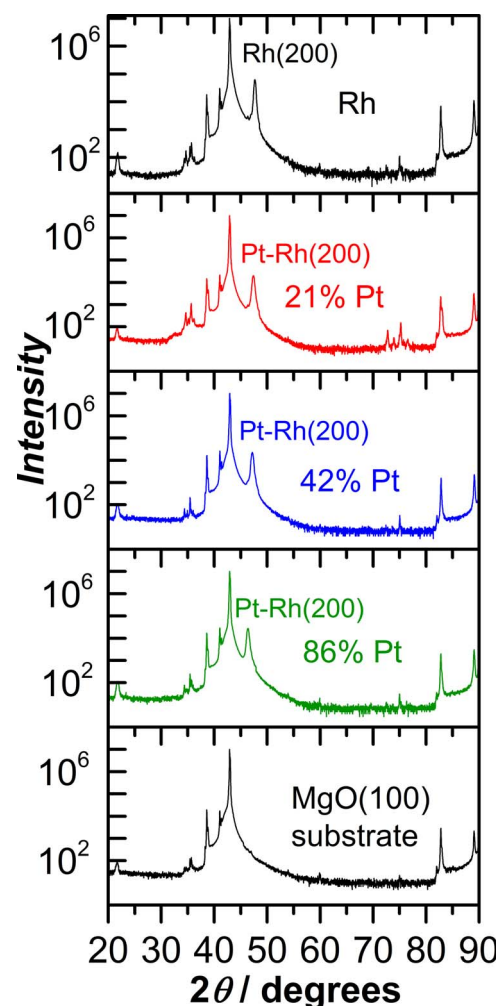


Fig. 1. X-ray diffraction patterns (XRD, Bragg-Brentano configuration) for thin-film Rh, $\text{Pt}_{21}\text{Rh}_{79}$, $\text{Pt}_{42}\text{Rh}_{58}$ and $\text{Pt}_{86}\text{Rh}_{14}$. The diffraction pattern of a representative $\text{MgO}(100)$ sample is also shown for the sake of comparison.

00-005-0685), corresponding to the (200) plane. Therefore, we can assign the peak in Fig. 1 to (200) planes, indicating that this is the predominant orientation of the Rh film. A lower 2θ value for the PLD deposited Rh film with respect to bulk Rh – which, by virtue of Bragg’s law, corresponds to a larger out-of-plane lattice parameter than for bulk Rh – was also previously observed for Pt [11]. In our previous report, it was explained in terms of elastic deformation arising from in-plane compressive epitaxial stress, ultimately due to the presence of a Ni buffering layer (the Ni lattice parameter is much smaller than that of Pt). The same explanation must hold true for Rh, too, since its lattice parameter is also larger than that of Ni. The preferential (100) orientation of the Rh thin layer can be corroborated by the absence of diffraction lines for other low-index planes, $2\theta = 40.99^\circ$ for (111) and 69.58° for (220), suggesting that such orientations are not featured in the Rh thin film, in line with our previous reports on the growth of (100) preferentially oriented Pt films [8,11].

The predominance of the (200) peak can also be observed for PtRh alloys, as highlighted in Fig. 2; more importantly, the peak position shifts towards lower 2θ values – in other words, towards the (200) reflection of a bare Pt film deposited by PLD, $2\theta_{\text{Pt}} = 46.2^\circ$ [11]. The monotonic decrease of 2θ for increasing Pt content in the PtRh alloys highlights the formation of a homogeneous alloy throughout the entire range of compositions. Kiesig fringes can be observed, indicating the crystalline quality of the deposit. The thickness of the deposited metal film was measured by XRR as described in the Experimental section,

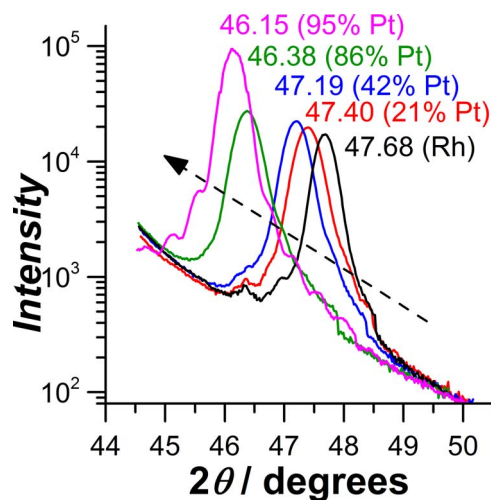


Fig. 2. Trend in the position of the XRD peak characteristic of the (002) reflection for thin-film Rh, $\text{Pt}_{21}\text{Rh}_{79}$, $\text{Pt}_{42}\text{Rh}_{58}$, $\text{Pt}_{86}\text{Rh}_{14}$ and $\text{Pt}_{95}\text{Rh}_5$.

and was found to vary between 13 and 17 nm. Such thickness was required for PtRh and Rh films to be sufficiently conductive and hence suitable for electrochemical measurements. The film average (in-plane) resistance was 25Ω , and so their voltammetric response was never distorted by ohmic drop.

While the response from XRD analyses invariably includes some contribution of deeper atomic layers, cyclic voltammetry is a powerful tool to investigate the electrode surface, also providing valuable insight into its crystalline orientation [44]. In fact, the distinctive appearance of the cyclic voltammogram (*i.e.* number of features, their multiplicity) is a proxy for the state of the electrode surface, while the position of the recorded peaks arise from the overall electronic properties of the entire electrode material [2]. Voltammetric evidence can thus corroborate the results from surface analysis techniques. Fig. 3 displays the voltammetric profile of a pure Rh thin film in 0.5 M H_2SO_4 in a restricted potential range, corresponding to the so-called ‘hydrogen adsorption/desorption region’. It is very informative to compare Fig. 3 to the voltammetric response of Rh(100) single crystals, described briefly hereafter. Defect-free Rh(100) single-crystal electrodes feature a pair of very sharp, spike-like oxidation-reduction signals located at *ca.* 0.14 V [46]

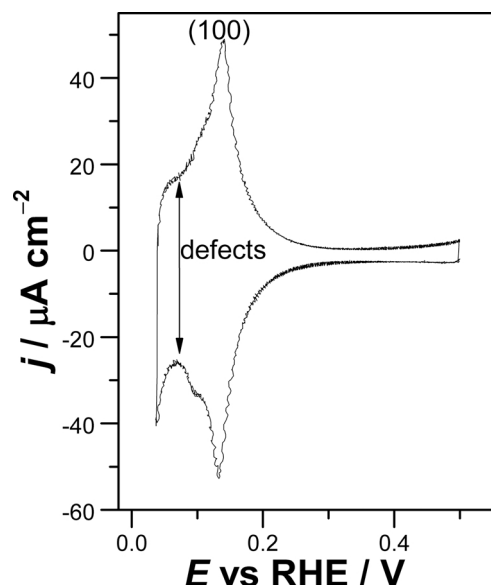


Fig. 3. Cyclic voltammetric profiles for (100) preferentially-oriented Rh in 0.5 M H_2SO_4 , $v = 20 \text{ mV s}^{-1}$.

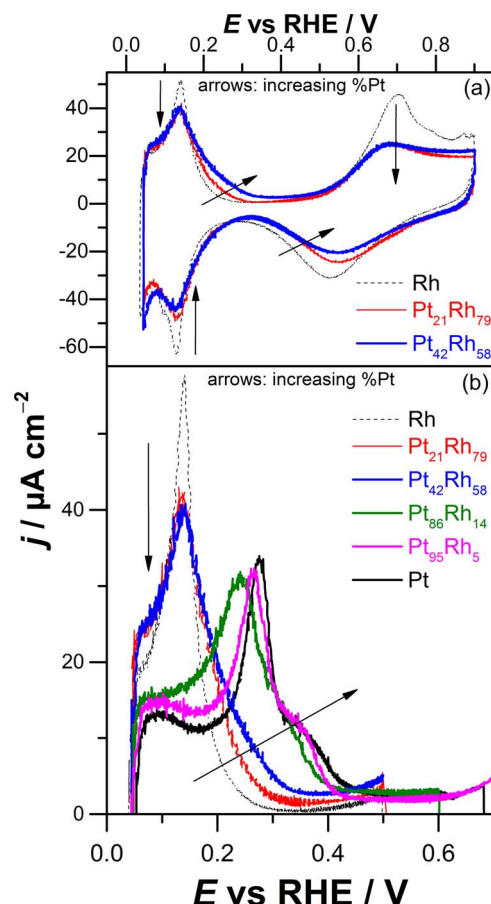


Fig. 4. Panel a: full-range cyclic voltammetric profiles for (100) preferentially-oriented Rh, $\text{Pt}_{21}\text{Rh}_{79}$ and $\text{Pt}_{42}\text{Rh}_{58}$ in 0.5 M H_2SO_4 , $v = 20 \text{ mV s}^{-1}$. Panel b: synopsis of the evolution of the hydrogen desorption region of the voltammograms recorded in 0.5 M H_2SO_4 for (100) preferentially-oriented Rh, $\text{Pt}_{21}\text{Rh}_{79}$, $\text{Pt}_{42}\text{Rh}_{58}$, $\text{Pt}_{86}\text{Rh}_{14}$, $\text{Pt}_{95}\text{Rh}_5$ and Pt, $v = 20 \text{ mV s}^{-1}$. In both panels, the arrows indicate an increasing Pt content.

when the scan rate is equal to 20 mV s^{-1} . The current trace to the right of the peaks (‘double-layer’ region) is narrow and featureless; on the left, the main peaks are clearly separated from hydrogen evolution. The magnitude of the current in this section of the voltammogram is slightly larger than in the double-layer region. The voltammogram in Fig. 3 can also be contrasted with Rh(110), which features hydrogen adsorption/desorption peaks shifted to lower potentials (*ca.* 0.11 V) and hence seamlessly merging with hydrogen evolution [46]. The overall shape of the voltammogram in Fig. 3 is in agreement with some of the features of Rh(100) single-crystal electrodes: the main voltammetric signals in Fig. 3 are located at 0.14 V and at 0.13 V for the anodic and cathodic peaks, respectively. On the other hand, they are not as sharp as those expected for a single-crystal Rh(100), with a visible shoulder accompanying the reduction peak. Although the hydrogen adsorption/desorption signals do not merge hydrogen evolution, the current in the region to the left of the peaks is larger than for a single-crystal Rh(100). The section of the blank voltammogram associated with Rh oxide formation also points to the presence of defects. Fig. 4a shows that the onset potential of Rh oxidation is *ca.* 0.5 V, with a large peak located at 0.7 V dominating the positive-going sweep. The signal associated with the reduction of Rh oxides is instead centred at 0.53 V in the return sweep. The voltammogram is stable within the potential limits chosen (below 0.9 V). The Rh profile in Fig. 4 combines some features of Rh (100) (shape and position of oxidation peak at 0.7 V) along with some characteristics of Rh(110), confirming that the (100) preferentially-oriented Rh surface is not defect-free. This is not surprising: in a previous report, we showed that the voltammetric response of a Pt film grown by

PLD onto MgO(100) is dominated by the features of *step* and *short terrace* (100) sites – h_2 and h_3 in the literature, respectively [11].

Voltammetry is also a choice technique to investigate alloys, as shown in Fig. 4. Panel 4b zooms in on the hydrogen desorption region, including the profiles of two additional alloys ($\text{Pt}_{86}\text{Rh}_{14}$ and $\text{Pt}_{95}\text{Rh}_5$) and of pure Pt(100), which is used as a reference throughout this paper. Alloying Pt and Rh brings about the following two major changes in the voltammetric profiles in blank H_2SO_4 :

- Progressive decrease of the hydrogen desorption signal of pure Rh, accompanied by its broadening towards higher potentials, i.e. towards the hydrogen desorption region of Pt(100) thin films (panel 4b).
- Lower tendency to oxidise, which is reflected in the displacement of the oxide reduction peak, shifting to higher potentials with respect to pure Rh for higher % Pt (panel 4a).

In other words, the electrochemical features will progressively evolve from those typical of pure Rh to those of pure Pt, as displayed clearly in Fig. 4b for the hydrogen desorption region. Our observations agree very well with trends in the evolution of voltammetric features reported previously for a series of bulk PtRh alloys [29], PtRh alloy nanoparticles [27], and well-ordered PtRh alloys formed on a Pt(100) single-crystal electrode by annealing [30]. In addition, we also point out that no voltammogram in Fig. 4 shows any peak located below 0.1 V – which would correspond to polycrystalline Rh deposits – thus ruling out the dissolution of large amounts of Rh and its re-deposition as disordered Rh islands during cyclic voltammetry.

Alloying PtRh exerts an even more profound effect on the electrocatalytic activity towards nitrate reduction, as summarised in Fig. 5. The voltammetric profile for nitrate reduction at a PLD-deposited Pt(100) electrode is shown as a reference in the top panel of Fig. 5: pure Pt is largely unable to reduce NO_3^- in H_2SO_4 . The starting potential was set at 0.08 V, and the potential was swept in the positive direction. The signal recorded retraces very closely the shape of the voltammogram in clean electrolyte (Fig. 4b). The response associated with NO_3^- reduction at Pt is weak, consisting of a current dip at 0.33 V in the forward scan. This corresponds to the sharp ‘spike’ which has been reported for Pt(100) electrodes [21] and vicinal stepped surfaces [48], arising from NO_3^- reduction at (100) sites after (partial) removal of H_{UPD} . Additional minor features were observed below 0.3 V in the return scan. On the other hand, Rh stands out as a much more active electrocatalyst for nitrate reduction, as known from several previous studies (refer to the Introduction). The reduction current maximum at $E = 0.10$ V and the overall shape of the current trace in Fig. 5b are in very good agreement with published reports on nitrate reduction at Rh [24,27]. When 21% Pt is alloyed with Rh, a significant anticipation of the onset potential is observed, the voltammetric profile shifting remarkably to the right ($\Delta E_{\text{onset}} = 55$ mV) with respect to pure Rh; an increase in the maximum current density was observed particularly in the return scan. Additionally, the voltammogram of nitrate reduction at the $\text{Pt}_{21}\text{Rh}_{79}$ alloy acquires a deep V-shaped aspect, characterised by a reduction peak located at *ca.* 0.15 V. This shape is also typical of the second alloy shown in Fig. 5, which features a higher Pt content (42%). If the voltammogram is converted into logarithmic units (by plotting E vs $\log|I|$), a linear fit (see Supporting information, Fig. S1) can be performed from 0.45 V to 0.25 V. The slope, commonly known as “Tafel slope”, is equal to 123.3 ± 0.5 mV. This value, which in electrochemical kinetics is associated with the fact that the first electron transfer is rate-determining, is typical of nitrate reduction at transition metal electrodes in acidic media [20]. The $\text{Pt}_{42}\text{Rh}_{58}$ alloy represents the optimal composition within the range studied: nitrate reduction is further enhanced with respect to $\text{Pt}_{21}\text{Rh}_{79}$, the peak current increasing from $-70 \mu\text{A cm}^{-2}$ to $-115 \mu\text{A cm}^{-2}$. A previous study on PtRh nanoparticles [27] seemed to suggest that the optimal composition for nitrate reduction was located at $\text{Pt}_{20}\text{Rh}_{80}$, which contrasts with our

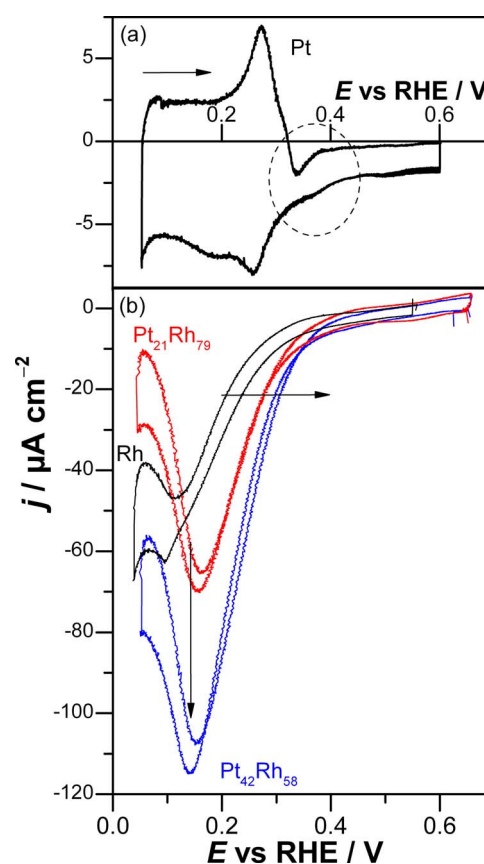


Fig. 5. Panel a: voltammetric profiles for the reduction of $0.01 \text{ M } \text{NO}_3^-$ at (100) preferentially-oriented Pt in $0.5 \text{ M } \text{H}_2\text{SO}_4$, $v = 5 \text{ mV s}^{-1}$. The arrow indicates the direction of potential scan. Panel b: cyclic voltammogram recorded for the reduction of $0.01 \text{ M } \text{NO}_3^-$ at (100) preferentially-oriented Rh, $\text{Pt}_{21}\text{Rh}_{79}$ and $\text{Pt}_{42}\text{Rh}_{58}$ in $0.5 \text{ M } \text{H}_2\text{SO}_4$, $v = 5 \text{ mV s}^{-1}$. The arrows indicate the effect of increasing Pt content on the voltammetric response.

findings. However, the authors were unable to explore the composition range corresponding to the ‘miscibility gap’ of PtRh alloys (no alloy was tested between $\text{Pt}_{20}\text{Rh}_{80}$ and $\text{Pt}_{70}\text{Rh}_{30}$), which instead is accessible to PLD, as explained in the Introduction. The reaction order for nitrate reduction for $\text{Pt}_{42}\text{Rh}_{58}$, was equal to 0.26 ± 0.02 (Figs. S2 and S3) at 0.14 V; reaction orders lower than 1 have been reported in the literature for nitrate reduction at noble metal electrodes, indicating that the rate-determining step involves an adsorbate [20].

Pt-rich PtRh alloys such as $\text{Pt}_{86}\text{Rh}_{14}$ (blank shown in Fig. 4b) and $\text{Pt}_{95}\text{Rh}_5$ become increasingly inactive towards nitrate reduction (Fig. S4), the voltammetric profile almost matching the current trace of pure Pt. In other words, the presence of a small amount of Rh is largely ineffective, while a comparable amount of Pt brings about a remarkable enhancement of nitrate reduction. As we shall see in the next section, this is also the case for Ir and PtIr alloys.

3.2. Ir and PtIr alloys: characterisation and electrocatalytic nitrate reduction

θ – 2θ Bragg-Brentano X-ray diffraction (XRD) patterns for pure Ir and PtIr alloys prepared onto MgO(100) are shown in Fig. 6. The composition was once more determined by EDX. If the XRD pattern of MgO is taken into account, the spectrum of a thin Ir deposit is dominated by the reflection at $2\theta = 47.2^\circ$. When compared to the value of $2\theta = 47.56^\circ$ reported for the (200) plane of bulk Ir (JCPDS card No. 00-001-1212), it indicates once more that the film is under epitaxial stress, as explained above in Section 3.1. Similar to the case of PtRh alloys, an increase in Pt content brings about a monotonic shift of the

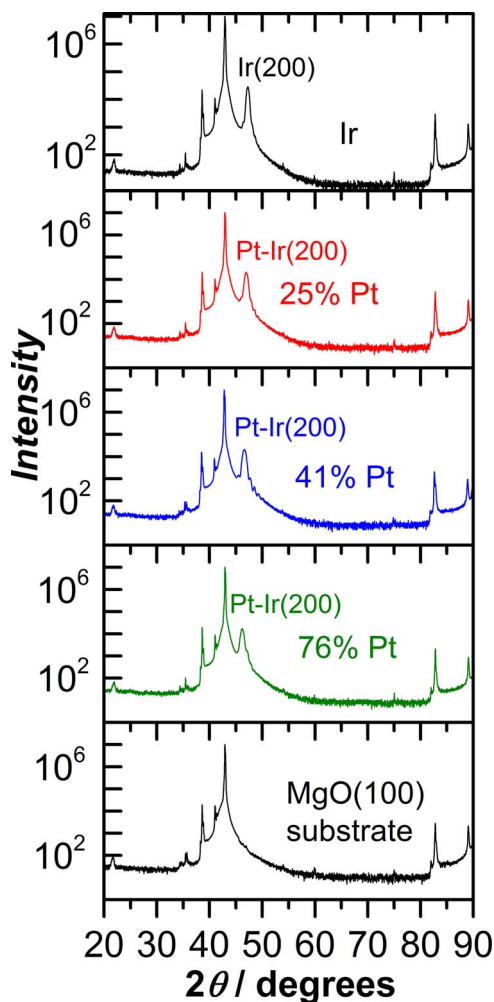


Fig. 6. X-ray diffraction patterns (XRD, Bragg-Brentano configuration) for thin-film Ir, Pt₂₅Ir₇₅, Pt₄₁Ir₅₉ and Pt₇₆Ir₂₄. The diffraction pattern of a representative MgO(100) sample is also shown for the sake of comparison.

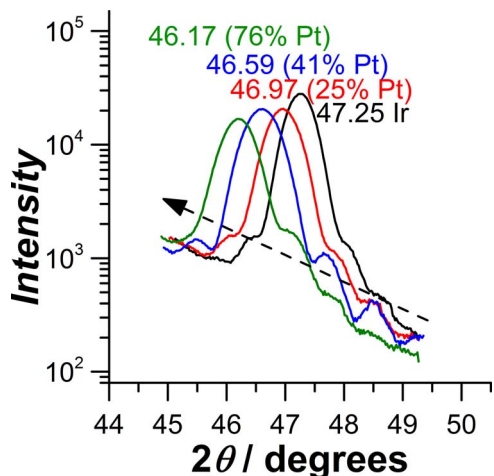


Fig. 7. Trend in the position of the XRD peak characteristic of the (002) reflection for thin-film Ir, Pt₂₅Ir₇₅, Pt₄₁Ir₅₉ and Pt₇₆Ir₂₄.

(002) reflection towards lower 2θ values (Fig. 7), thus confirming successful alloying of the two metals at all compositions.

The formation of an Ir deposit with a preferential (100) orientation of the Ir surface can be corroborated once more by cyclic voltammetry: the voltammograms of stepped Ir single crystal surfaces with (100)

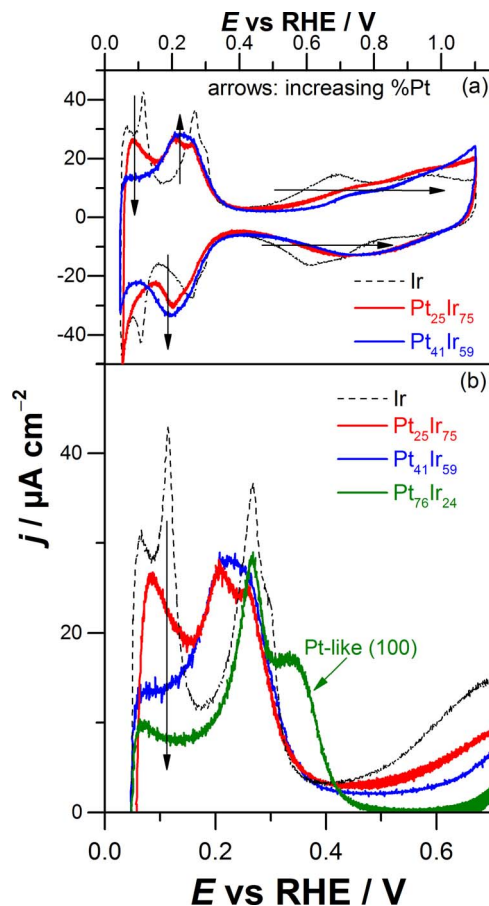


Fig. 8. Panel a: full-range cyclic voltammetric profiles for (100) preferentially-oriented Ir, Pt₂₅Ir₇₅ and Pt₄₁Ir₅₉ in 0.5 M H₂SO₄, $v = 20 \text{ mV s}^{-1}$. Panel b: synopsis of the evolution of the hydrogen desorption region of the voltammograms recorded in 0.5 M H₂SO₄ for (100) preferentially-oriented Ir, Pt₂₅Ir₇₅, Pt₄₁Ir₅₉ and Pt₇₆Ir₂₄, $v = 20 \text{ mV s}^{-1}$. In both panels, the arrows indicate an increasing Pt content.

terraces are available in the literature [49]. Fig. 8a displays the voltammetric profile of a pure Ir film in 0.5 M H₂SO₄. First, a couple of sharp signals can be observed at 0.11 V, overlapping on the background current associated with the onset of H₂ evolution. These combined features can be ascribed to hydrogen adsorption/desorption at short Ir (100) terraces close to (111) steps – as reported for a Ir(311) electrode [49]. In addition, also Ir(100) domains in the vicinity of (110) steps will contribute to the peaks at 0.11 V. At a higher potential, a broad peak, including a large shoulder, dominates the voltammogram at 0.27 V. This is the potential region in which hydrogen adsorption/desorption processes take place at Ir(100), giving rise to a sharp doublet [42,49]. In our case, the broadening is a direct consequence of the presence of (100) domains of smaller size than in the case of a single-crystal Ir(100) electrode: the closest well-defined surface is Ir(610). Further information on the surface orientation can be gained by observing the potential region in which adsorption of oxygenated species occurs on Ir ($E > 0.5$ V). Fig. 8 displays a broad feature developing over a broad potential range, between 0.6 and 1 V, with multiple peaks. In particular, the multiple signals centred around 0.7 V are typically associated with Ir(100) [42,49], while defects contribute with a featureless background current.

Alloying Ir with Pt brings about significant changes in the voltammetric profile, as shown in Fig. 8:

- As in the case of PtRh alloys, Pt contributes to delaying the formation of oxygen-containing adsorbates, and eventually, of metal oxidation.

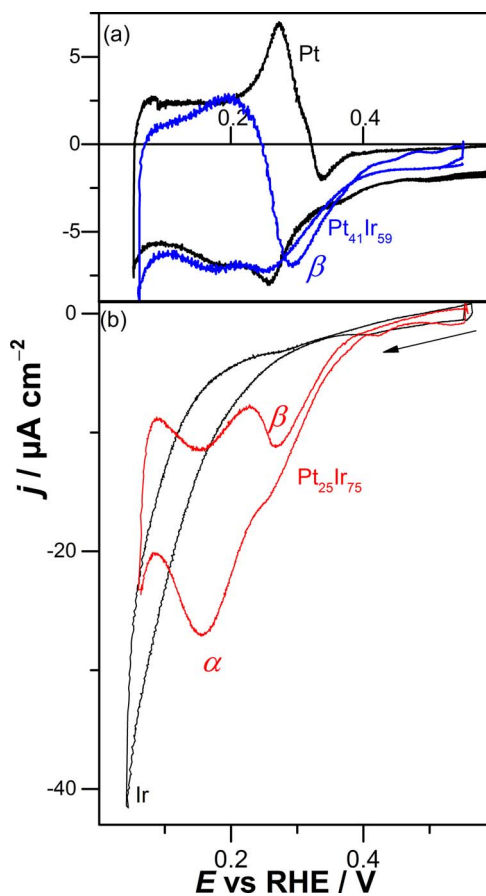


Fig. 9. Panel a: voltammetric profiles for the reduction of 0.01 M NO_3^- at (100) preferentially-oriented Pt and Pt₄₁Ir₅₉ in 0.5 M H_2SO_4 , $v = 5 \text{ mV s}^{-1}$. Panel b: cyclic voltammogram recorded for the reduction of 0.01 M NO_3^- at (100) preferentially-oriented Ir and Pt₂₅Ir₇₅ in 0.5 M H_2SO_4 , $v = 5 \text{ mV s}^{-1}$. The arrow indicates the direction of potential scan.

- In addition, the hydrogen adsorption/desorption region is also affected by increasing proportions of Pt. Unfortunately, the overlap of the H_{UPD} signals of Pt(100) and Ir(100) short terraces, both located at 0.27 V, impairs a clear-cut visualisation of the evolution of the voltammetric response towards hydrogen adsorption for the PtIr series.

When increasing amounts of Pt are alloyed to Ir, the voltammetric features observed below 0.2 V for pure Ir lose intensity (Pt₂₅Ir₇₅) before disappearing completely (Pt₄₁Ir₅₉). On the other hand, as we emphasised above, the evolution of the (100) H_{UPD} peak at ca. 0.27 V is more complex. Pt₂₅Ir₇₅ displays a broad doublet, centred at 0.24 V, which evolves into a broad single peak for Pt₄₁Ir₅₉. Finally, a Pt-like character appears for the Pt-rich alloy, Pt₇₆Ir₂₄, as shown by the presence of a voltammetric feature associated with long Pt(100) terraces.

PtIr alloys also display a peculiar response towards nitrate reduction, although the gain in electrocatalytic activity is not as remarkable as that observed for PtRh. This is certainly due, in part, to the lower intrinsic nitrate reduction activity of Ir with respect to Rh [20]. The voltammetric trace recorded for a pure Ir film is shown in Fig. 9b. A featureless reduction current characterises Ir in both scan directions, with an onset potential of 0.31 V. Comparable signals have been reported for the reduction of NO_3^- [20], NO_2^- and NO [37] at bulk polycrystalline Ir electrodes in 0.5 M H_2SO_4 . The maximum current is lower than for pure Rh ($-40 \mu\text{A cm}^{-2}$ vs $-60 \mu\text{A cm}^{-2}$), and it is attained at a very low potential, at which nitrate reduction is likely to overlap with hydrogen evolution. Instead, Pt₂₅Ir₇₅ features an anticipated reduction wave starting from 0.4 V ($\Delta E_{\text{onset}} = 90 \text{ mV}$ with

respect to pure Ir) and culminating in the main reduction peak at 0.15 V (α henceforth). A shoulder (β) at 0.26 V appears in both the forward and the return sweep. Interestingly, α is located at the same potential as the most intense reduction peak described above for Pt₂₁Rh₇₉ and Pt₄₂Rh₅₈. On the other hand, β is closer to peak potential of the ‘spike’ typical of Pt. The peak current of α is lower than the value recorded for pure Ir; however, the position of α ensures that there is no interference from impending hydrogen evolution. A further increase of the Pt content of the PtIr alloy (Pt₄₁Ir₅₉ in Fig. 9b) causes a significant decrease in the response towards nitrate reduction, contrary to the additional gain in reduction current described above for Pt₄₂Rh₅₈. Moreover, Pt₄₁Ir₅₉ is characterised by a weak reduction signal in the same region as β , and the α peak is completely suppressed. The detrimental effect of increasing the Pt content of the alloy further is confirmed by the voltammetric trace for nitrate reduction at a Pt₇₆Ir₂₄ (not shown in Fig. 8 for ease of reading – refer to Fig. S5), which is almost identical to the voltammogram of nitrate reduction at pure Pt in Fig. 9a. Our results are in stark contrast with the literature on nitrate reduction at bulk PtIr alloys (see Introduction); however, this is not at all surprising, since bulk, polycrystalline alloys were exclusively employed, and the Ir-rich composition range was not explored due to the intrinsic limitations associated with conventional alloying procedures [36].

3.3. Poison removal by CO adsorption

In this section, we will report on the effect of CO adsorption on electrode poisoning during nitrate reduction. This experiment was inspired by the mechanism of the well-known three-way catalyst for automotive applications [50] and by a previous study by Nakata et al. reporting on the displacement of NO and nitrate adsorbed at a Pt electrode by CO [51]. It showed that a significant increase in the intensity of the nitrate reduction current can be obtained in the first cycles following CO stripping. Poisoning is a known issue affecting electrodes which catalyse most of the reactions of the nitrogen cycle: this has been demonstrated in particular for ammonia oxidation [10,35,52] and the reductive stripping of NO [37,53], and it is ascribed to the buildup of stable adsorbed species, such as adsorbed nitrogen atoms, N_{ads} . During repeated cycling in the potential region of nitrate reduction, a loss of activity was observed for all the electrode materials studied in this work (see Figs. S6 and S7). This is by no means surprising, since NO is an intermediate of nitrate reduction. We will focus on a particular case, Pt₂₅Ir₇₅ (the comparison between the first and the second voltammetric cycles is shown in Fig. S7). Fig. 10 displays the voltammetric profile recorded for this alloy after adsorption of CO: as expected for a fully-blocked surface, all features in the H_{UPD} region are suppressed. The oxidation of adsorbed CO, performed at 20 mV s⁻¹, begins at 0.6 V and take place as a broad peak which clearly overlaps with oxide formation (see Fig. 8). The shape is similar to the CO stripping profile reported in the literature for Ir [41] and Ir(100) [54]. After reversing the potential, the scan rate was switched to 5 mV s⁻¹ (for the sake of comparison) prior to the potential region where NO_3^- reduction takes place. The voltammetric profile is now dominated by a very intense, sharp signal centred at 0.145 V (called peak α in section 3.2), which can be compared to the current trace recorded for nitrate reduction *prior* to CO stripping, also shown in Fig. 10: the gain in reduction current thanks to CO stripping is fourfold. This remarkable increase in peak current for α seems to indicate that this signal is associated with nitrate reduction at Ir, which is alloy component more likely to be poisoned. In this sense, the experiment in Fig. 10 also provided valuable mechanistic information, highlighting once more how alloying brings about a modulation of the reactivity of the component surface metals atoms. This is further supported by the observation that CO is *largely ineffective* in reversing the poisoning on pure Ir (Fig. S8): Pt-free Ir(100) is poised to re-adsorb, and dissociate, NO during the return sweep after CO oxidation, leading to a minimal net increase in NO_3^- reduction current even after CO adsorption.

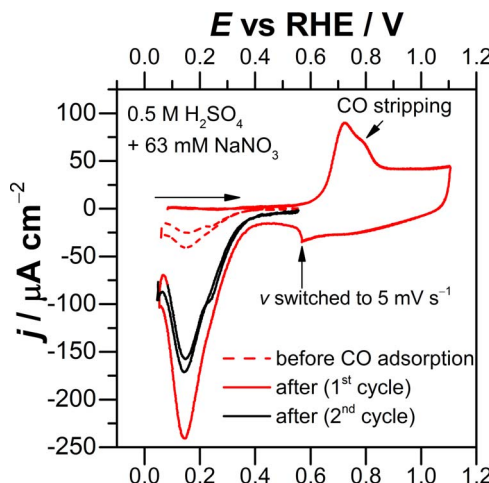


Fig. 10. Voltammetric profiles for CO stripping and NO_3^- reduction at $\text{Pt}_{25}\text{Ir}_{75}$ in a $0.5 \text{ M H}_2\text{SO}_4$ solution containing 63 mM NaNO_3 . The red dashed line shows the signal for NO_3^- reduction prior to the adsorption of CO. $v = 20 \text{ mV s}^{-1}$ for CO stripping until the potential marked with the vertical arrow, then $v = 5 \text{ mV s}^{-1}$. (For interpretation of the references to colour in this figure legend, the reader is referred to the web version of this article.)

Unfortunately, Fig. 10 also shows that the gain in reduction current was partially lost in the second cycle after CO removal, although, the peak current of α still remained remarkably higher than before CO adsorption.

Poisoning removal by CO adsorption was also observed for electrodes of the PtRh series (see Fig. S9 for $\text{Pt}_{42}\text{Rh}_{58}$). In this case, the alloy displays a less severe poisoning than PtIr or Ir, and the gain in activity after CO stripping is not as striking as in Fig. 10.

To conclude this section, we would like to add a word of caution: bimetallic alloys are dynamic systems [2] and the adsorption of CO does entail the risk of bringing about a change in the alloy composition through segregation of the alloy component that binds CO more strongly [55]. This is the risk inherent in poisoning removal by CO adsorption. Nevertheless, neither a change in the position of the H_{UPD} features nor the appearance of new features was observed upon CO adsorption in blank (nitrate-free) electrolyte, which seems to rule out any CO-induced change to alloy composition.

3.4. General discussion

This section will first present the correlations existing between the various observable quantities characterizing PtM alloys and their catalytic performance towards nitrate reduction in H_2SO_4 . Secondly, a rationalisation of the trends in performance will be discussed, also pointing out its intrinsic limitations.

3.4.1. Nitrate reduction at PtM alloys: trends in voltammetric data

This section will first focus on PtRh for sake of clarity: in fact, the two component metals feature typical hydrogen adsorption/desorption peaks located at very different potentials (see Fig. 3), which greatly simplifies data analysis. Fig. 11 presents an overview of the parameters associated with hydrogen adsorption and nitrate reduction (obtained from voltammetry) for the $\text{Pt}_x\text{Rh}_{(100-x)}$ series as a function of alloy composition. Fig. 11a shows the relationship between the “centre of gravity of the hydrogen desorption region” and the Pt content of the alloy. In this work we define the centre of gravity as the potential at which the hydrogen desorption charge attains 50% of its total amount, as obtained from the integration of the voltammograms in Fig. 4b. This parameter was chosen because it simultaneously takes into account the position, the shape and the intensity of H_{UPD} peaks, thus proving extremely useful when alloys display identical position of the main hydrogen desorption signal, but different overall profiles (*i.e.* $\text{Pt}_{21}\text{Rh}_{79}$ vs

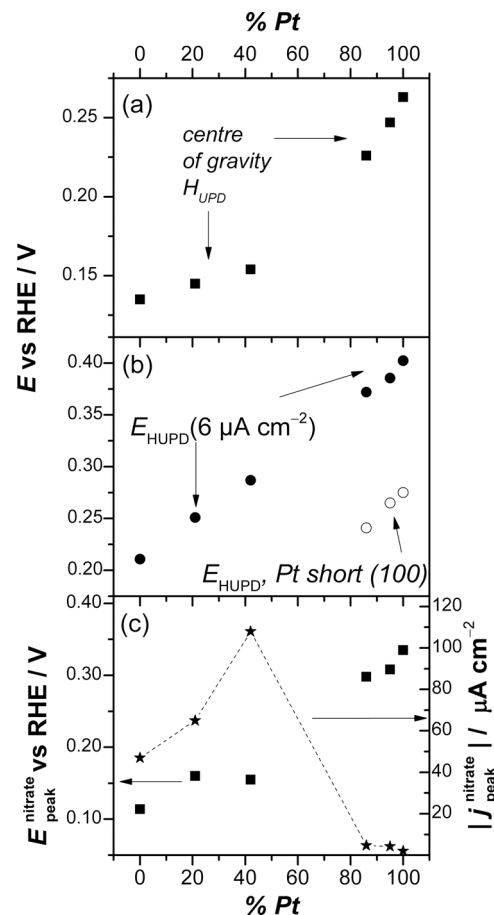


Fig. 11. Overview of the trends in voltammetric data shown in Figs. 3, 4, 5 and S4 as a function of Pt content in the PtRh series. Panel a: plot of the centre of gravity of hydrogen desorption (defined as the potential at which 50% of the hydrogen desorption charge is recorded). Panel b: trend in the tail of the hydrogen desorption region, expressed as the potential corresponding to a current density of $6 \mu\text{A cm}^{-2}$, (full circles); trend in the potential of the peak associated with hydrogen desorption from $\text{Pt}(100)$ short terraces (empty circles). Panel c: potential of the main nitrate reduction peak (left y-axis, full squares); absolute value of the peak current density for the main nitrate reduction signal recorded during the positive-going sweep (right y-axis, stars linked by dashed line).

$\text{Pt}_{42}\text{Rh}_{58}$). The choice of referring to the 50% of the hydrogen desorption charge, though seemingly arbitrary, was motivated by previous reports on nitrate reduction at a $\text{Pt}(100)$ single-crystal electrode [21,48] and vicinal surfaces [48]: the peak for nitrate reduction during the anodic scan occurred at a potential corresponding situated approximately at the centre of the hydrogen UPD region. The most important feature of Fig. 11a is the monotonic dependence of the centre of gravity on % Pt, indicating that the shift from Rh-like character to Pt-like character takes place gradually throughout the entire $\text{Pt}_x\text{Rh}_{(100-x)}$ series. Secondly, Fig. 11a highlights a Rh-rich region, in which the centre of gravity rises gently, and a Pt-rich region characterised by a steeper slope – as if the effect on H_{UPD} of alloying Pt with an excess of Rh were milder than the inverse. Finally, Fig. 11a suggests that there could be a critical % Pt, approximately at 60%, corresponding to the transition from Rh-like to Pt-like character. In summary, Fig. 11a indicates that – for metals as different as Pt and Rh – a parameter as simple as the centre of gravity is a useful proxy for the “character” of the alloy (*i.e.* being Pt- or Rh-like). Fig. 11b shows two other plots: the first is a trend of the “tail” of hydrogen desorption, arbitrarily expressed as the potential corresponding to a current density twice as much as the double-layer current in Fig. 4b, $E(j = 6 \mu\text{A cm}^{-2})$, as a function of % Pt. It can be seen that $E(j = 6 \mu\text{A cm}^{-2})$ depends linearly on % Pt. However, what matters most in Fig. 11b is once more the monotonic rise of $E(j = 6 \mu\text{A cm}^{-2})$ with increasing % Pt throughout the entire $\text{Pt}_x\text{Rh}_{(100-x)}$

series. In addition, Fig. 11b also shows the position of the voltammetric peak corresponding to H_{UPD} at (100) step sites (from Fig. 4b) for pure Pt and the two Pt-rich alloys prepared in this study. Similar to E ($j = 6 \mu\text{A cm}^{-2}$), this parameter displays a monotonic upward shift as a function of increasing % Pt. The evolution in the hydrogen adsorption properties of the alloys can be interpreted for instance in terms of the potential of zero (total/free) charge, which differs greatly for the two metals: it has been reported that the (apparent) potential of zero total charge of Pt(100) is 0.38 V in 0.1 M H₂SO₄, while it is as low as 0.15 V for Rh(100) in the same electrolyte [56].

Fig. 11c summarises the trends in the main peak of nitrate reduction (intensity and position). Interestingly, the peak potential associated with nitrate reduction tends to increase for higher % Pt, just as the parameters of hydrogen desorption, with a remarkable outlier: Pt₄₂Rh₅₈, which is also the most active alloy.

PtIr is instead an unfortunate case for data analysis, since a major H_{UPD} signal of the (100) surface occurs at the same potential for the two composing metals. The trends of the voltammetric features as a function of % Pt are shown in the Supporting information for the sake of comparison (Fig. S10). Only peak β is analysed (see Fig. 9 for the notation), because peak α disappears when the platinum content increased. On the other hand, we emphasise that the most intense reduction peak recorded at the overall “best” alloy (Pt₂₅Ir₇₅, combining enhanced activity and lower overpotential with respect to Ir), α , is located at *exactly the same potential* as the nitrate reduction peak recorded for both Rh-rich PtRh alloys, $0.15 < E_{\text{peak}} < 0.16$ V (for a concentration of 0.01 M NO₃⁻ and a scan rate of 5 mV s⁻¹). In other words, there seem to exist a quite restricted potential window in which the highest nitrate reduction current is obtained for PtIr and PtRh alloys.

To further investigate the underpinnings of this apparently optimal potential for nitrate reduction at PtRh and PtIr alloys, we present the combined data for both series in Fig. 12. The plot shows the peak current for the main nitrate reduction peak (in the return scan) as a function of the absolute value of the difference between the apparent optimal nitrate reduction potential (0.155 V) and the centre of gravity of the H_{UPD} region. The correlation displayed by the data points in Fig. 12 is particularly intriguing: it suggests that an enhanced nitrate reduction activity can be obtained by tuning the properties of the alloy so that the potential at which half of the surface becomes free from hydrogen will precisely coincide with the potential of optimal nitrate reduction. This is not as elusive as it may seem at a first glance: since nitrate competes with hydrogen (and bisulphate) for free surface sites,

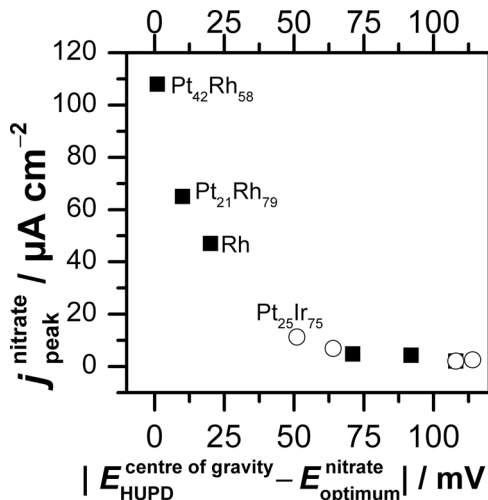
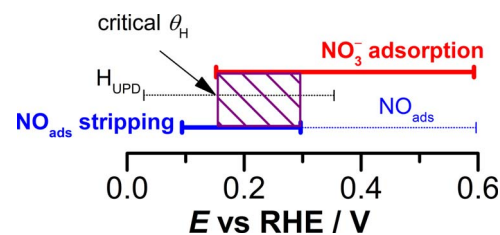


Fig. 12. Trend in the peak current density for the main signal of nitrate reduction (recorded in the positive-going sweep) as a function of the absolute value of the difference between the centre of gravity of hydrogen desorption and the optimum potential for nitrate reduction, equal to 0.155 V. The PtRh and the PtIr series are combined and plotted as full squares and empty circles, respectively.



Scheme 1. Simplified depiction of the competing/simultaneous surface processes at a generic metal electrode during nitrate reduction. Red line: potential window of nitrate adsorption, which begins at a potential corresponding to a sufficiently low hydrogen coverage – labelled as “critical θ_H ” and marked by a black arrow. Blue full line: potential window of fast reduction of adsorbed NO – the dashed blue line indicates the potential range of stability of NO_{ads}. The purple dashed area arises from the two requirements of nitrate reduction and corresponds to the region in which nitrate reduction is expected to occur at the fastest rate. (For interpretation of the references to colour in this figure legend, the reader is referred to the web version of this article.)

the centre of gravity of H_{UPD} can be seen as a rough estimation of the lowest potential at which nitrate can replace hydrogen. This is the first key point: nitrate adsorption is a precondition for nitrate reduction to occur – and adsorbed nitrate is indeed involved in the rate-determining step, as shown by the fact that the reaction order with respect to NO₃⁻ is lower than unity (Fig. S3 and [20]). In the second place, we also need to recall that nitrate reduction involves adsorbed NO at sub-saturation coverages [21], which is both an intermediate and a poison: its removal determines to a great extent the potential at which nitrate reduction achieves its maximum rate. While it is true that in this work we did not actually study NO reduction at the preferentially-oriented alloys, we believe that it is logical to refer to literature data on NO reduction at noble metal electrodes and extend these results to their alloys. Chronoamperometry and voltammetric data [14,22,23,53,54,57–60] indicate that the electrochemical stripping of NO adsorbed at Pt, Rh or Ir is most effective between 0.3 and 0.1 V. It is thus clear that the reaction rate of nitrate reduction at any given electrode will be optimised in the potential range *simultaneously* ensuring a sufficient coverage of nitrate (requirement 1) and a sufficiently fast reduction of NO_{ads} (requirement 2) – as depicted graphically in Scheme 1. The existence of these two requirements, the first being more stringent than the second, unfortunately seems to place strict restrictions on the latitude for the development of metallic electrocatalysts showing high activity at low overpotential for nitrate reduction, calling for the combination of non-metallic and metallic catalysts [61].

3.4.2. Rationalising the trends: electronic effects and strain

To rationalise the experimental trends discussed above, we shall rely on general considerations on the electronic structure of metal alloys, because no specific computational data are available for these well-ordered alloys.

It is well-known that the trends in reactivity and catalytic activity of alloys can be discussed in terms of three main concepts [2,62]: *ensemble* effects (*i.e.* the presence of specific surface sites enhancing a particular reaction), *ligand* effects (*i.e.* the modification in electronic levels as a consequence of alloying) and *strain* effects (*i.e.* the modification in lattice parameter due to alloying). Ligand effects, in particular, are often addressed by focussing on the *d*-band centre. In this respect, an upward shift of the *d*-band centre with respect to the native level of pure Pt is expected to favour the adsorption of oxygen species [63], which is particularly important for the adsorption of nitrate, since it binds to the metal surface through one or more oxygen atoms [51]. Both Rh and Ir display a higher *d*-band centre than Pt [63], and therefore the ability to adsorb nitrate could be tuned by alloying Pt with each of the two group 9 metals. A stronger adsorption of nitrate will then exert a significant impact on the reaction rate, because this adsorbate is directly involved in the rate-determining step, as recalled above.

At the same time, an excessively strong adsorption of reactants or intermediates is also detrimental as it could lead to surface poisoning. In the specific case of nitrate reduction, adsorbed NO can dissociate into its atomic constituents: N_{ads} fragments are known to be particularly recalcitrant, often causing irreversible poisoning of the catalytic surface – *cfr.* for instance the case of ammonia oxidation cited in Section 3.3 [14]. However, NO does not tend to dissociate into N_{ads} equally for all metal surfaces. One can predict that the likelihood of NO dissociation increases on metals to the left and to the bottom of the *d*-block [17]. For instance, it has been shown that polycrystalline Ir electrodes tend to suffer from severe poisoning upon adsorption of NO [37] which binds very strongly to Ir [17]. NO dissociative adsorption has been highlighted for a Ir(100) electrode by infrared spectroscopy [54]. Similarly, Rh is also affected by poisoning, though to a lower extent than Ir, as observed during the reductive stripping of adsorbed NO [53]. In addition, irreversible poisoning was shown to occur preferentially at the (100) facets of Rh [59]. On the other hand, NO does not dissociate upon adsorption at Pt under electrochemical conditions, and the profile of clean polycrystalline Pt can be recovered by stripping adsorbed NO [14,64]. Pt(100) is also a peculiar surface for NO reduction: a computational study combining *ab initio* DFT with kinetic Monte Carlo suggested that N_{ads} from N–O bond breaking is promptly hydrogenated at Pt(100) [23], further preventing poisoning. Since the removal of adsorbed NO is the potential-determining step of nitrate reduction, alloying some Pt to Rh or Ir is a viable strategy to lower the overpotential for NO stripping while avoiding the poisoning associated with NO adsorption at both Rh and Ir.

Finally, it is extremely important to bear in mind that the alloys prepared in this study always feature a certain degree of strain, as shown by XRD data. *Strain effects* could also influence the position of the *d*-band centre, and hence the reactivity of the alloy surface. However, we exclude that strain can play a key role in determining the trends in catalytic activity for nitrate reduction. In fact, all alloys, regardless of their composition, are expected to be strained to a similar extent by the presence of the Ni buffer layer, Ni having a much smaller lattice parameter than Pt, Rh or Ir. Thus, all PLD Pt-M films are under similar compressive *in-plane* strain and tensile *out-of-plane* strain because of this mismatch and we do not expect the strain to play a key role in determining the trends shown in Section 3.4.1.

It is intriguing to compare nitrate reduction to its counterpart, ammonia oxidation: optimal activities for the latter reaction were achieved with *Pt-rich* Pt–Ir alloys [10], while it is *Ir- and Rh-rich* alloys that display a better performance for the reduction of NO_3^- . Adsorption of N and O species can provide common ground to draw a unified picture of trends in performance of Pt–M alloys for these two antipodal reactions of the nitrogen cycle. By alloying a small amount of Ir to Pt, an upward tuning of the *d*-band centre of Pt(100) will likely occur, facilitating OH adsorption. This will further enhance the intrinsically high catalytic activity of pristine Pt(100) towards the oxidation of NH_3 . However, an excessive upward shift of the *d*-band will eventually bind OH_{ads} and N_{ads} too strongly, inhibiting ammonia oxidation. As for nitrate reduction, the high-lying intrinsic *d*-band of Rh is instrumental in facilitating the adsorption of NO_3^- through the oxygen atoms and facilitating its rate-determining reduction to NO_2^- . Nevertheless, the Rh and Ir *d*-bands need to be tuned to lower values by Pt in order to sidestep excessively strong adsorption of N- or O- species, such as fragments of NO_{ads} , and to avoid poisoning.

4. Conclusion

Pulsed laser deposition was employed to deposit (100) preferentially-oriented thin films of Ir, Rh, and of PtRh and PtIr alloys. The voltammetric features for hydrogen adsorption/desorption and oxide formation in 0.5 M H_2SO_4 highlighted the gradual change in the electrochemistry of the alloys as a function of the content of the two alloyed metals. The electrocatalytic activity of these thin-film electrodes

towards the reduction of nitrate was studied by cyclic voltammetry, evidencing that the addition of 21–42% Pt to Rh brings about an enhancement of the catalytic activity of the host metal and a decrease of the overpotential for the reduction of nitrate. This is all the more surprising, since Rh is generally considered the most active metal for this reaction. Similarly, the performance of Ir was improved by alloying it with 25% Pt; in addition, it was shown that CO adsorption and stripping was particularly effective in removing the poisoning associated with nitrate reduction at Pt₂₅Ir₇₅. Finally, we described the trends in the electrochemical features observed for both the PtRh and PtIr series, which highlighted the existence of a narrow potential window, centred at 0.155 V, corresponding to maximum nitrate reduction activity for PtM alloys under the experimental conditions of this study. To rationalise this observation, a descriptive parameter was introduced, the centre of gravity of the hydrogen desorption region, defined as the potential at which 50% of hydrogen has been desorbed from the surface. In this way, it was shown that the catalytic activity is inversely proportional to the difference between the centre of gravity of hydrogen desorption and the optimal potential for nitrate reduction. This is not mere coincidence: adsorbed nitrate is involved in the rate-determining step, and the centre of gravity is a proxy for the potential at which the surface is able to adsorb nitrate. When nitrate adsorption is operative within the potential window of fast reduction of intermediate NO_{ads} (between 0.1 and 0.3 V for most transition metals), an optimum for nitrate reduction will be observed. Finally, these trends were placed within the context of the ligand and strain effects in bimetallic electrocatalysts.

Acknowledgements

This work was supported by the Natural Sciences and Engineering Research Council of Canada (NSERC) and the Canada Research Chair program. A.W. gratefully acknowledges the support of NSERC through an Undergraduate Student Research Award (USRA).

Appendix A. Supplementary data

Supplementary data associated with this article can be found, in the online version, at <http://dx.doi.org/10.1016/j.apcatb.2017.08.081>.

References

- [1] F. Calle-Vallejo, M.T.M. Koper, A.S. Bandarenka, Tailoring the catalytic activity of electrodes with monolayer amounts of foreign metals, *Chem. Soc. Rev.* 42 (2013) 5210–5230.
- [2] J.E. Mueller, P. Krtil, L.A. Kibler, T. Jacob, Bimetallic alloys in action: dynamic atomistic motifs for electrochemistry and catalysis, *Phys. Chem. Chem. Phys.* 16 (2014) 15029–15042.
- [3] H. Kobayashi, K. Kusada, H. Kitagawa, Creation of novel solid-solution alloy nanoparticles on the basis of density-of-states engineering by interelement fusion, *Acc. Chem. Res.* 48 (2015) 1551–1559.
- [4] J. Rodriguez, Physical and chemical properties of bimetallic surfaces, *Surf. Sci. Rep.* 24 (1996) 223–287.
- [5] D.H. Lowndes, D.B. Geohegan, A.A. Puretzky, D.P. Norton, C.M. Rouleau, Synthesis of novel thin-film materials by pulsed laser deposition, *Science* 273 (1996) 898–903.
- [6] E. Iriissou, F. Laplante, S. Garbarino, M. Chaker, D. Guay, Structural and electrochemical characterization of metastable PtAu bulk and surface alloys prepared by crossed-beam pulsed laser deposition, *J. Phys. Chem. C* 114 (2010) 2192–2199.
- [7] R. Imbeault, D. Reyter, S. Garbarino, L. Roue, D. Guay, Metastable Au_xRh_{100-x} thin films prepared by pulsed laser deposition for the electrooxidation of methanol, *J. Phys. Chem. C* 116 (2012) 5263–5270.
- [8] J. Galipaud, C. Roy, M.H. Martin, S. Garbarino, L. Roue, D. Guay, Electrooxidation of ammonia at tuned (100)Pt surfaces by using epitaxial thin films, *ChemElectroChem* 2 (2015) 1187–1198.
- [9] Y. Yamabe-Mitarai, T. Aoyagi, T. Abe, An investigation of phase separation in the Ir–Pt binary system, *J. Alloy Compd.* 484 (2009) 327–334.
- [10] R. Imbeault, D. Finkelstein, D. Reyter, S. Garbarino, L. Roue, D. Guay, Kinetically stable Pt_xIr_{100-x} alloy thin films prepared by pulsed laser deposition: oxidation of NH_3 and poisoning resistance, *Electrochim. Acta* 142 (2014) 289–298.
- [11] N. Sacré, G. Hufnagel, J. Galipaud, E. Bertin, S.A. Hassan, M. Duca, L. Roué, A. Ruediger, S. Garbarino, D. Guay, Pt thin films with nanometer-sized terraces of (100) orientation, *J. Phys. Chem. C* 121 (2017) 12188–12198.

- [12] S.E. Temmel, E. Fabbri, D. Pergolesi, T. Lippert, T.J. Schmidt, Tuning the surface electrochemistry by strained epitaxial Pt thin film model electrodes prepared by pulsed laser deposition, *Adv. Mater. Interfaces* 3 (2016).
- [13] S.E. Temmel, E. Fabbri, D. Pergolesi, T. Lippert, T.J. Schmidt, Investigating the role of strain toward the oxygen reduction activity on model thin film Pt catalysts, *ACS Catal.* 6 (2016) 7566–7576.
- [14] V. Rosca, M. Duca, M.T. de Groot, M.T.M. Koper, Nitrogen cycle electrocatalysis, *Chem. Rev.* 109 (2009) 2209–2244.
- [15] M. Duca, M.T.M. Koper, Powering denitrification: the perspectives of electrocatalytic nitrate reduction, *Energy Environ. Sci.* 5 (2012) 9726–9742.
- [16] J.O. Bockris, J. Kim, Electrochemical treatment of low-level nuclear wastes, *J. Appl. Electrochem.* 27 (1997) 623–634.
- [17] W.A. Brown, D.A. King, NO chemisorption and reactions on metal surfaces: a new perspective, *J. Phys. Chem. B* 104 (2000) 2578–2595.
- [18] N. Sheppard, C. De la Cruz, A systematic review of the application of vibrational spectroscopy to the determination of the structures of no adsorbed on single-crystal metal surfaces, *PCCP* 12 (2010) 2275–2284.
- [19] S.N. Pronkin, P.A. Simonov, V.I. Zaikovskii, E.R. Savinova, Model Pd-based bimetallic supported catalysts for nitrate electroreduction, *J. Mol. Catal. A: Chem.* 265 (2007) 141–147.
- [20] G.E. Dima, A.C.A. de Vooy, M.T.M. Koper, Electrocatalytic reduction of nitrate at low concentration on coinage and transition-metal electrodes in acid solutions, *J. Electroanal. Chem.* 554–555 (2003) 15–23.
- [21] G.E. Dima, G.L. Beltramo, M.T.M. Koper, Nitrate reduction on single-crystal platinum electrodes, *Electrochim. Acta* 50 (2005) 4318–4326.
- [22] I. Katsounaros, M.C. Figueiredo, X. Chen, F. Calle-Vallejo, M.T.M. Koper, Structure- and coverage-sensitive mechanism of the NO reduction on platinum electrodes, *ACS Catal.* 7 (2017) 4660–4667.
- [23] H.-J. Chun, V. Apaja, A. Clayborne, K. Honkala, J. Greeley, Atomistic insights into nitrogen-cycle electrochemistry: a combined DFT and kinetic Monte Carlo analysis of NO electrochemical reduction on Pt(100), *ACS Catal.* (2017) 3869–3882.
- [24] J. Yang, P. Sebastian, M. Duca, T. Hoogenboom, M.T.M. Koper, pH dependence of the electroreduction of nitrate on Rh and Pt polycrystalline electrodes, *Chem. Commun.* 50 (2014) 2148–2151.
- [25] O.A. Petrii, T.Y. Safanova, Zero charge potentials and work function of rhodium, *J. Electroanal. Chem.* 688 (2013) 336–348.
- [26] F. Calle-Vallejo, J.I. Martinez, J.M. Garcia-Lastra, J. Rossmeisl, M.T.M. Koper, Physical and chemical nature of the scaling relations between adsorption energies of atoms on metal surfaces, *Phys. Rev. Lett.* 108 (2012) 5.
- [27] P. Rodriguez, F.D. Tichelaar, M.T.M. Koper, A.I. Yanson, Cathodic corrosion as a facile and effective method to prepare clean metal alloy nanoparticles, *J. Am. Chem. Soc.* 133 (2011) 17626–17629.
- [28] M.S. Ureta-Zanartu, M. Montenegro, J.H. Zagal, Methanol electro-oxidation on Pt-Rh alloys in acid medium, *Bol. Soc. Chilena Quim.* 46 (2001) 209–216.
- [29] W. Tokarz, H. Siwek, P. Piela, A. Czerwiński, Electro-oxidation of methanol on Pt-Rh alloys, *Electrochim. Acta* 52 (2007) 5565–5573.
- [30] L. Fang, F.J. Vidal-Iglesias, S.E. Huxter, G.A. Attard, A study of the growth and CO electrooxidation behaviour of PtRh alloys on Pt(100) single crystals, *J. Electroanal. Chem.* 622 (2008) 73–78.
- [31] Y.W. Lee, K.W. Park, Pt-Rh alloy nanodendrites for improved electrocatalytic activity and stability in methanol electrooxidation reaction, *Catal. Commun.* 55 (2014) 24–28.
- [32] ASM handbook: Volume 3: Alloy phase diagrams, 10th edition.
- [33] R. Palaniappan, D.C. Ingram, G.G. Botte, Hydrogen evolution reaction kinetics on electrodeposited Pt-M (M = Ir, Ru, Rh, and Ni) cathodes for ammonia electrolysis, *J. Electrochem. Soc.* 161 (2014) E12–E22.
- [34] S. Le Vot, L. Roue, D. Belanger, Synthesis of Pt-Ir catalysts by coelectrodeposition: application to ammonia electrooxidation in alkaline media, *J. Power Sources* 223 (2013) 221–231.
- [35] N.N. Fomena, S. Garbarino, J. Gaudet, L. Roué, D. Guay, Nanostructured Pt surfaces with Ir submonolayers for enhanced NH₃ electro-oxidation, *ChemElectroChem* 4 (2017) 1327–1333.
- [36] S. Ureta-Zanartu, C. Yáñez, Electroreduction of nitrate ion on Pt, Ir and on 70:30 Pt:Ir alloy, *Electrochim. Acta* 42 (1997) 1725–1731.
- [37] M. Duca, B. van der Klugt, M.T.M. Koper, Electrocatalytic reduction of nitrite on transition and coinage metals, *Electrochim. Acta* 68 (2012) 32–43.
- [38] A.C.A. De Vooy, M.T.M. Koper, R.A. Van Santen, J.A.R. Van Veen, The role of adsorbates in the electrochemical oxidation of ammonia on noble and transition metal electrodes, *J. Electroanal. Chem.* 506 (2001) 127–137.
- [39] S.R. Bharadwaj, S.N. Tripathi, M.S. Chandrasekharaiyah, The Ir-Pt (iridium-platinum) system, *J. Phase Equilib.* 16 (1995) 460–464.
- [40] M.H. Martin, J. Galipaud, A. Tranchot, L. Roué, D. Guay, Measurements of hydrogen solubility in Cu_xPd_{100-x} thin films, *Electrochim. Acta* 90 (2013) 615–622.
- [41] M.A. Montero, J.L. Fernández, M.R. Gennero de Chialvo, A.C. Chialvo, Kinetic study of the hydrogen oxidation reaction on nanostructured iridium electrodes in acid solutions, *J. Phys. Chem. C* 117 (2013) 25269–25275.
- [42] S. Motoo, N. Furuya, Hydrogen and oxygen-adsorption on Ir(111), Ir(100) and Ir(110) planes, *J. Electroanal. Chem.* 167 (1984) 309–315.
- [43] Q.Q. Xu, U. Linke, R. Bujak, T. Wandlowski, Preparation and electrochemical characterization of low-index rhodium single crystal electrodes in sulfuric acid, *Electrochim. Acta* 54 (2009) 5509–5521.
- [44] V. Climent, J.M. Feliu, Thirty years of platinum single crystal electrochemistry, *J. Solid State Electr.* 15 (2011) 1297–1315.
- [45] R. Gómez, M.J. Weaver, Reduction of nitrous oxide on iridium single-crystal electrodes, *Langmuir* 18 (2002) 4426–4432.
- [46] R. Gómez, J.M. Feliu, A. Aldaz, M.J. Weaver, Validity of double-layer charge-corrected voltammetry for assaying carbon monoxide coverages on ordered transition metals: comparisons with adlayer structures in electrochemical and ultrahigh vacuum environments, *Surf. Sci.* 410 (1998) 48–61.
- [47] A. Ahmadi, R.W. Evans, G. Attard, Anion surface interactions. 1. Perchlorate decomposition and sulfate adsorption hysteresis studied by voltammetry, *J. Electroanal. Chem.* 350 (1993) 279–295.
- [48] E.B. Molodkina, I.G. Botryakova, A.I. Danilov, J. Souza-Garcia, J.M. Feliu, Mechanism of nitrate electroreduction on Pt(100), *Russ. J. Electrochem.* 48 (2012) 302–315.
- [49] N. Furuya, S. Koide, Hydrogen adsorption on iridium single-crystal surfaces, *Surf. Sci.* 226 (1990) 221–225.
- [50] P. Granger, V.I. Parvulescu, Catalytic NO_x abatement systems for mobile sources: from three-way to lean burn after-treatment technologies, *Chem. Rev.* 111 (2011) 3155–3207.
- [51] K. Nakata, Y. Kayama, K. Shimazu, A. Yamakata, S. Ye, M. Osawa, Surface-enhanced infrared absorption spectroscopic studies of adsorbed nitrate, nitric oxide, and related compounds 2: Nitrate ion adsorption at a platinum electrode, *Langmuir* 24 (2008) 4358–4363.
- [52] D.A. Finkelstein, E. Bertin, S. Garbarino, D. Guay, Mechanistic similarity in catalytic N₂ production from NH₃ and NO₂ at Pt(100) thin films: toward a universal catalytic pathway for simple N-containing species, and its application to in situ removal of NH₃ poisons, *J. Phys. Chem. C* 119 (2015) 9860–9878.
- [53] M. Duca, B. van der Klugt, M.A. Hasnat, M. Machida, M.T.M. Koper, Electrocatalytic reduction of nitrite on a polycrystalline rhodium electrode, *J. Catal.* 275 (2010) 61–69.
- [54] R. Gomez, M.J. Weaver, Electrochemical infrared studies of monocrystalline iridium surfaces. 3. Adsorbed nitric oxide and carbon monoxide as probes of Ir(100) interfacial structure, *J. Phys. Chem. B* 102 (1998) 3754–3764.
- [55] E. Christoffersen, P. Stoltze, J.K. Norskov, Monte Carlo simulations of adsorption-induced segregation, *Surf. Sci.* 505 (2002) 200–214.
- [56] O.A. Petrii, Zero charge potentials of platinum metals and electron work functions (review), *Russ. J. Electrochem.* 49 (2013) 401–422.
- [57] A.C.A. de Vooy, M.T.M. Koper, R.A. van Santen, J.A.R. van Veen, Mechanistic study on the electrocatalytic reduction of nitric oxide on transition-metal electrodes, *J. Catal.* 202 (2001) 387–394.
- [58] R. Gomez, M.J. Weaver, Electrochemical infrared studies of monocrystalline iridium surfaces. Part 2: Carbon monoxide and nitric oxide adsorption on Ir(110), *Langmuir* 14 (1998) 2525–2534.
- [59] A. Rodes, R. Gomez, J.M. Perez, J.M. Feliu, A. Aldaz, On the voltammetric and spectroscopic characterization of nitric oxide adlayers formed from nitrous acid on Pt(h,k,l) and Rh(h,k,l) electrodes, *Electrochim. Acta* 41 (1996) 729–745.
- [60] R. Gomez, A. Rodes, J.M. Perez, J.M. Feliu, FTIRS and electrochemical characterization of the NO adlayer generated by immersion of a Rh(111) electrode in an acidic solution of nitrite, *J. Electroanal. Chem.* 393 (1995) 123–129.
- [61] M. Duca, J.R. Weeks, J.G. Fedor, J.H. Weiner, K.A. Vincent, Combining noble metals and enzymes for relay cascade electrocatalysis of nitrate reduction to ammonia at neutral pH, *ChemElectroChem* 2 (2015) 1086–1089.
- [62] A. Groß, Reactivity of bimetallic systems studied from first principles, *Top. Catal.* 37 (2006) 29–39.
- [63] F.H.B. Lima, J. Zhang, M.H. Shao, K. Sasaki, M.B. Vukmirovic, E.A. Ticianelli, R.R. Adzic, Catalytic activity-d-band center correlation for the O₂ reduction reaction on platinum in alkaline solutions, *J. Phys. Chem. C* 111 (2007) 404–410.
- [64] M. Duca, V. Kavvadia, P. Rodriguez, S.C.S. Lai, T. Hoogenboom, M.T.M. Koper, New insights into the mechanism of nitrite reduction on a platinum electrode, *J. Electroanal. Chem.* 649 (2010) 59–68.